Reaction Chemistry & Engineering

# The role of gas flow distributions on CO2 mineralization within monolithic cemented composites: Coupled CFD-factorial design approach

| | |
|---|---|
| Journal: | *Reaction Chemistry & Engineering* |
| Manuscript ID | RE-ART-11-2020-000433.R1 |
| Article Type: | Paper |
| Date Submitted by the Author: | 28-Dec-2020 |
| Complete List of Authors: | Mehdipour, Iman; University of California Los Angeles Henry Samueli School of Engineering, Department of Civil and Environmental Engineering<br>Falzone, Gabriel; University of California Los Angeles, Civil and Environmental Engineeering<br>Prentice, Dale; University of California Los Angeles, Civil and Environmental Engineering<br>Neithalath, Narayanan; Arizona State University, School of Sustainable Engineering and the Built Environment<br>Simonetti, Dante; University of California at Los Angeles, Department of Chemical and Biomolecular Engineering<br>Sant, Gaurav; University of California, Los Angeles, Department of Civil and Environmental Engineering |
| | |

*Revised for Submission to Reaction Chemistry & Engineering (December 2020)*

# The role of gas flow distributions on $CO_2$ mineralization within monolithic cemented composites: Coupled CFD-factorial design approach

*Iman Mehdipour ([*],[†]), Gabriel Falzone ([*],[†]), Dale Prentice ([*],[†]), Narayanan Neithalath ([‡]), Dante Simonetti ([†],[§]), Gaurav Sant ([*],[†],[**],[††],[&])*

**ABSTRACT**

The carbonation kinetics of monolithic cementing composites are strongly affected by gas transport which is, in turn, influenced by microstructural resistances and the presence of liquid water within pore networks. The non-uniform gas flow distribution within the $CO_2$ mineralization reactor can impart mass transfer resistance in the monolith microstructure, which affects the uptake of $CO_2$ ("carbonation") of the cementing composites. This paper demonstrates how the gas spatial distribution (velocity and flow rate; quantified by CFD analysis) and processing conditions (temperature, relative humidity, and flow rate; quantified by factorial design) affect drying and carbonation, and in turn, the engineering properties of a representative 'monolithic' carbonate-cemented concrete component (i.e., herein concrete masonry unit: CMUs, also known as concrete block). It is shown that the gas flow distribution affects drying front penetration and results in moisture and carbonation gradients within the monolith. Particularly, variations in drying kinetics caused by non-uniformity of the contacting gas velocity impose gradients in moisture saturation, which results in increasing microstructural resistance to $CO_2$ transport. The resultant non-uniform carbonate-mineral formation (i.e., carbonate cementation), if not controlled, can produce gradients in mechanical properties and may alter failure patterns upon loading. These insights inform the optimal design of gas flow distribution systems and processing conditions within $CO_2$ mineralization reactors for the manufacturing of low-$CO_2$ concrete components using $CO_2$-dilute industrial flue gas streams.

**Keywords:** *$CO_2$ mineralization; flow distribution; kinetics; CFD; strength; process design.*

[*] Laboratory for the Chemistry of Construction Materials (LC[2]), Department of Civil and Environmental Engineering, University of California, Los Angeles, CA 90095, USA
[†] Institute for Carbon Management (ICM), University of California, Los Angeles, CA 90095, USA
[‡] School of Sustainable Engineering and the Built Environment, Arizona State University, Tempe, AZ 85287, USA
[§] Department of Chemical and Biomolecular Engineering, University of California, Los Angeles, CA 90095, USA
[**] Department of Materials Science and Engineering, University of California, Los Angeles, CA 90095, USA
[††] California Nanosystems Institute (CNSI), University of California, Los Angeles, CA 90095, USA

[&] Corresponding author: G. Sant, Phone: (310) 206-3084, Email: gsant@ucla.edu

## INTRODUCTION AND BACKGROUND

Low-carbon cementation agents produced by *in situ* $CO_2$ mineralization ("mineral carbonation reactions") offer a promising alternative to ordinary portland cement (OPC).[1–3] $CO_2$ mineralization relies upon the reaction of dissolved $CO_2$ with inorganic alkaline reactants to precipitate mineral carbonate (e.g., $CaCO_3$), which binds proximate particles and results in cementation.[2,4,5] Herein, a shape-stabilized concrete *green body*, that is composed of a mixture of reactants, water, and mineral aggregates, is exposed to $CO_2$ borne in industrial flue gas streams or concentrated $CO_2$. Such $CO_2$ mineralization and utilization are foundational to decarbonize cement production by creating a waste-to-value or carbon-to-value economy (e.g., by valorizing waste $CO_2$ borne in flue gases and alkaline solid wastes such as fly ashes), reducing the costs and liabilities associated with waste management, and promoting the principles of circular economy.[1,6,7] Generally speaking, $CO_2$ mineralization allows the production of construction components that feature equivalent engineering attributes to their ordinary portland cement (OPC) based counterparts while featuring a much smaller embodied carbon intensity (eCI). The reduction in eCI of such carbonated concrete products is attributable to: (i) the utilization of $CO_2$ from a waste emissions stream during production and (ii) the avoidance of $CO_2$ emissions by the partial substitution of OPC by industrial solid wastes (e.g., fly ash) and alkaline solids. Portlandite ($Ca(OH)_2$) is a particularly attractive alkaline solid for use in such applications because it can be produced at a substantively lower temperature than OPC,[8] while offering a remarkable $CO_2$ uptake capacity for a non-porous inorganic reactant (59 mass %).[2]

The carbonation kinetics of alkaline solid reactants and cementing composites are affected by the gas processing conditions including: temperature $T$, relative humidity $RH$, $CO_2$ concentration [$CO_2$], and gas flow rate ($Q$).[9,10] For monoliths, the carbonation kinetics increase with decreasing $RH$ and elevated $T$; so long as a critical $RH$ is exceeded.[3] Reducing $RH$ decreases the quantity of water within the pore spaces (i.e., which affects the so-called moisture saturation, $S_w$), thereby easing $CO_2$ transport into and within the microstructure. This is because, in a porous body, the gas diffusivity through the microstructure is inversely proportional to the microstructural resistance factor (i.e., as described by the porosity and $S_w$).[11] Achieving the optimal carbonation conditions within plug-flow style reactors requires precise control of the gas processing conditions, flow rates, and flow distributions because the non-uniform gas flow and velocity can detrimentally impact moisture removal and drying and carbonation kinetics by imparting mass transfer resistance, which leads to $S_w$ gradients within monolithic components. Such $S_w$ gradients result in non-uniform $CO_2$ uptake across the monolith's volume and gradients in properties (e.g., porosity).

Computational fluid dynamics (CFD) has been widely used for evaluating fluid flow patterns,[12] and mixing processes[13] to understand gas flow distributions and heat- and mass-transfer[14] to inform the design of chemical reactors.[15,16] Although the importance of the gas velocity on gas-solid reactions has been extensively studied, developing reactor designs and process models for systems that promote the carbonation reactions of cementitious composites is difficult because of the non-uniform boundary conditions at the gas-solid interface and unsteady state (dynamic) nature of the process. Therefore, this study uncovers the role of gas flow distribution and processing conditions on $CO_2$ mineralization reaction for a representative monolith (i.e., herein

concrete masonry unit: CMUs, also known as concrete block) that is carbonated within a plug-flow style reactor at ambient pressure. As such, first, CFD simulations are used to link the velocity and spatial distributions of gas flowing across the monolith's surfaces within a $CO_2$ mineralization reactor to drying front penetration and $CO_2$ diffusion and their effects on the measured bulk $CO_2$ uptake across monolith's volume. Second, the impact of stiffness/strength gradients resulting from the non-uniform carbonate-mineral formation on the overall mechanical performance of the concrete block is discussed and analyzed via finite element modeling (FEM). Finally, for the optimal gas flow configuration, a factorial design approach is used to identify optimal gas processing conditions (*RH*, *T*, and *Q*) that best facilitates gas diffusion within microstructure and enhance bulk $CO_2$ uptake across the monolith's volume. Taken together, the outcomes offer new understanding to design optimal $CO_2$ mineralization reactors and to identify the optimal gas processing routes to enable the scalable production of low-eCI concrete components using waste-$CO_2$ borne flue gas streams.

## MATERIALS AND METHODS

**Materials and specimen preparation:** A mixture of inorganic reactants (e.g., the *binder*), inert fine aggregates (sand), and water was used to make "dry-cast" formulations suitable for the fabrication of concrete blocks; the monolith geometry considered herein. The reactants used consisted of commercially available portlandite ($Ca(OH)_2$) powder (Standard Hydrated Lime, Mississippi Lime Co.), ASTM C150-compliant ordinary portland cement (Type I/II OPC),[17] and ASTM C618-compliant fly ash (Class F, $m_{CaO}$ = 2.18 mass % as determined via X-ray fluorescence).[18] The $Ca(OH)_2$ had a purity of 94 % ± 2 % (by mass) with the remainder being composed of $CaCO_3$ as determined by thermogravimetric analysis (TGA).

A concrete block making machine (Stonemaker DM100) was used to produce structural "load-bearing" concrete blocks.[19] The overall dimensions of the blocks were 200 mm x 200 mm x 400 mm ($w \times h \times L$) with face-shell and web thicknesses of 32 mm and 25 mm, respectively (see SI: Figure S1) yielding a surface-to-volume ratio of 0.081 $mm^{-1}$. The concrete block mixture was formulated with 10 mass % dry binder, 4.5 mass % water with the remainder consisting of mineral aggregates. The mixing and forming process of the fresh concrete blocks are described in the SI. After forming, the fresh concrete blocks were pre-cured at $T$ = 21 ± 1 °C for 12 h to gain green strength (compressive strength $\sigma_c$ = 1.5 ± 0.5 MPa) to enable handling and loading into the carbonation reactor. Based on the water content and the forming method, the pore water saturation $S_w$ of the concrete blocks prior to carbonation was on the order of 0.62 ± 0.02 (unitless) determined as per ASTM C140.[20]

**Carbonation processing**: A bench-scale $CO_2$ mineralization system was fabricated consisting of gas mixing equipment, a humidification chamber, and a carbonation reactor (see Figure 1a). The gas processing parameters were examined over a range of temperatures (20 °C ≤ $T$ ≤ 80 °C), relative humidities (10 % ≤ $RH$ ≤ 60 %), and gas flow rates (0.10 slpm ≤ $Q$ ≤ 4.92 slpm). In all cases, the $CO_2$ concentration [$CO_2$] of the gas stream was fixed at 12.5 ± 0.2 % [v/v], as confirmed using gas chromatography (GC; F0818, Inficon) to simulate the $CO_2$-dilute flue gas stream of a coal-fired power plant.[21] The gas mixture was prepared by mixing air and $CO_2$ streams at prescribed flow rates using calibrated mass flow controllers (MFC; Alicat). The mixed

gas was humidified by bubbling through gas washing bottles that were placed in an oven. The humidified gas stream was then passed into the carbonation reactor, which was formed from a lidded stainless steel batch can (600 mm × 450 mm × 300 mm; $l \times w \times h$) and wrapped with heating-tape and insulated to regulate temperature. In longitudinal and transverse flow configurations (Figure 1b), the gas inlet and outlet (6.35 mm diameter) were positioned in the middle of the reactor's sidewalls, while for top flow, the gas inlet was located in the middle of the reactor's lid and the longitudinal outlet was used.

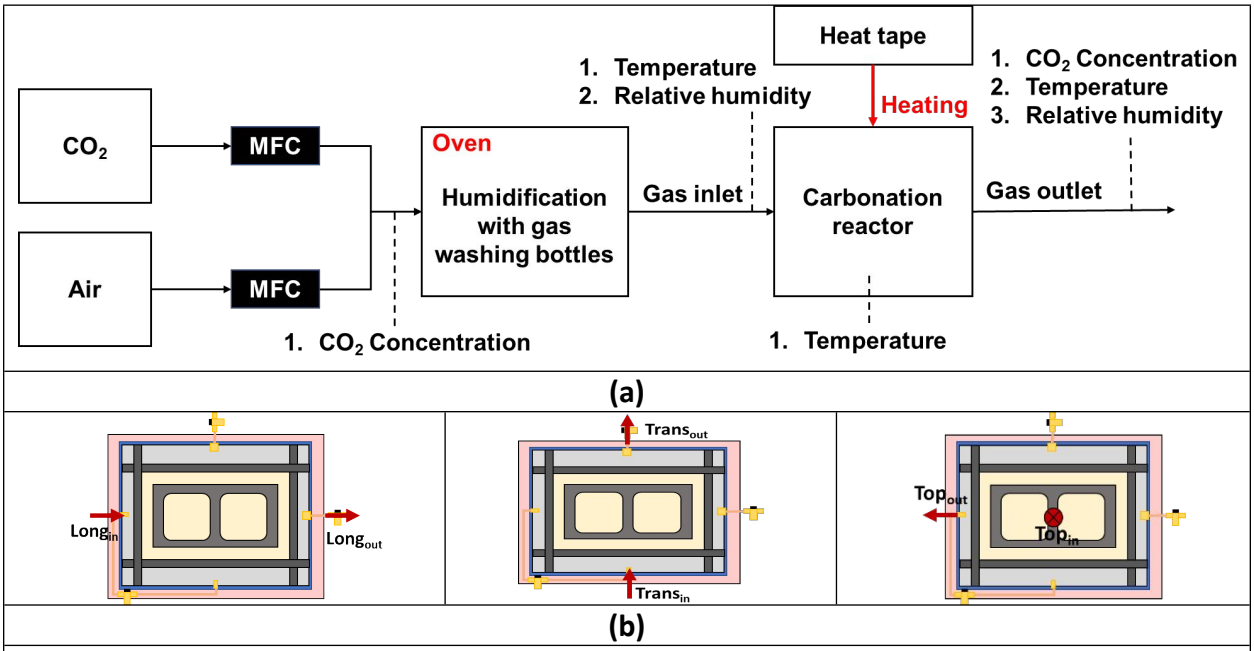


**Figure 1: (a)** A schematic of the bench-scale $CO_2$ mineralization system used for block carbonation including gas mixing equipment, a humidification chamber, a carbonation reactor, and relevant instrumentation. **(b)** A schematic depicting the inlet and outlet positions of the gas stream for longitudinal, transverse, and top flow configurations. The arrows in **(b)** indicate the inlet and outlet positions. The top flow configuration used the longitudinal outlet since the concrete block was placed on a solid base that precludes true top-to-bottom flow within the reactor.

To assess the effect of gas flow distribution on carbonation, various gas flow configurations (e.g., longitudinal, transverse, and top flow) were used as shown in Figure 1(b). Second, to systematically evaluate the interactions between gas processing parameters ($T$, $RH$, and $Q$) for a single flow configuration, a factorial Design-of-Experiments (DoE) approach was implemented. The design variables and their corresponding lower and upper bounds are presented in Table S2 in SI. The significance of variables and their interactions were determined by the analysis of variance (ANOVA) approach using least-squares fitting. A non-linear regression analysis was used to derive statistical prediction models and develop response surfaces. The results of statistical models were then integrated into a multivariable optimization algorithm to determine the optimal parameters that satisfy the performance targets.[22] Here, for defined

targets, the desirability functions $d_i$ are obtained and simultaneously optimized to determine their best combination as quantified by the overall desirability $D$ function[23]:

$$D = (d_1^{r_1} \times d_2^{r_2} \times d_3^{r_3} \times \ldots \times d_n^{r_n})^{1/\sum r_i} \quad \textbf{[Eq. 1]}$$

where $n$ is the number of individual responses in the optimization, and $r_i$ refers to the relative importance of each property, which varies from 1 to 5, reflecting the smallest to the highest degree of importance, respectively. And, $d_i$ ranges between 0 (i.e., least desired response) and 1 (i.e., most desired response).[23] Hereafter, the concrete blocks were dried by exposure to flowing air to achieve different initial $S_w$ prior to the carbonation process. The temperature, relative humidity, and flow rate during the drying step were equivalent to those applied during carbonation, with the exception of using an air stream (i.e., [$CO_2$] = 0.04 %) during drying rather than simulated flue gas ([$CO_2$] = 12.5 %) that was used during carbonation.

**Material characterization:** The concrete block was sampled across different sections including: each side (long dimension), each face (short dimension), and the web (i.e., the interior wall between the two hollows) to assess the variations in $CO_2$ uptake across different sections (see SI: Figure S2). For sampling, a rotary hammer with a 6 mm drill-bit was used to extract powders through the entirety of the section's thickness. The total $CO_2$ uptake ($CO_{2,total}$) within a block was estimated as a mass average of each section's $CO_2$ uptake as:

$$\mathrm{CO}_{2,\mathrm{total}} = \sum_{i=1}^{n=5} C(24h)_i (g_{CO_2}/g_{reactants}) \times m_i \quad \textbf{[Eq. 2]}$$

where, $C(24h)_i$ is the 24-h $CO_2$ uptake of the i$^{th}$ section (i.e., side, face, or web) and $m_i$ refers to the mass fraction of a section in relation to the entire block mass. Thermogravimetric analysis (TGA: STA 6000, Perkin Elmer) was used to assess the extent of $CO_2$ uptake following ASTM C1872.[24] Around 50 mg of powder was heated from 35 °C to 975 °C at a rate of 15 °C/min in aluminum oxide crucibles under ultra-high purity $N_2$ gas purge at a flow rate of 20 mL/min. The carbonate content was quantified by assessing the mass loss associated with $CaCO_3$ decomposition over the temperature range of 550 °C to 950 °C, normalized by the initial mass of reactants ($g_{CO2}/g_{reactants}$; reactants: portlandite, fly ash, and OPC) within the solid. It should be noted that the $CO_2$ uptake accounted for the initial quantity of carbonates that were present in the precursor materials prior to the carbonation process. In addition to carbonate content, the non-evaporable water content ($w_n$, mass %) was calculated as the mass loss over the temperature range of 105 °C to 975 °C, excluding the mass loss from the decomposition of $CaCO_3$ and $Ca(OH)_2$ to estimate the extent of cement (OPC) hydration.[35,36]

The net area compressive strengths of the concrete blocks were measured in accordance with ASTM C140[20] under uniaxial monotonic displacement-controlled loading using a hydraulic jack with a capacity of 800 kN. The bearing plates used for compression testing were large enough to cover the contact surfaces of the block entirely to distribute the load evenly, and rigid enough (100 mm thick) to eliminate plate bending that can cause non-uniform stresses.[20] To characterize the variations of carbonate mineral formation, the porosity and compressive strength of the different block's sections (i.e., sides, web, and faces) were determined. Representative samples (50 mm × 50 mm × 25 mm; $l \times w \times t$) were cut from the middle of each

section of the concrete block using a low-speed saw. The total porosity and pore saturation level of samples were quantified using a vacuum saturation method[27] and the compressive strengths of the samples were measured as per ASTM C39.[28] Finally, to assess the effects of gas processing conditions on the transport properties (diffusion), the total moisture diffusion coefficient (i.e., the sum of liquid water and water vapor diffusion coefficients) during drying was estimated using Fick's 2nd law.[29] Herein, the sides of the sectioned samples (50 mm × 50 mm × 25 mm; *l* × *w* × *t*) were double-sealed using adhesive-backed aluminum tape to ensure 1D gas transport (exposed surfaces: 50 mm × 50 mm; *l* × *w*).

## COMSOL© MULTIPHYSICS: CFD AND FEM SIMULATIONS

CFD simulations were used to assess the effects of gas flow configurations on the spatial distribution and velocity of contacting gas across the concrete block's surfaces within the carbonation reactor. The gas flow analysis was carried out using the $k-\omega$ turbulence model,[30] which is suitable for gas velocity analysis near solid wall regions.[31,32] The Reynolds number $Re$ based on inlet diameter $d_{inlet}$ and inlet velocity $V_{inlet}$ was calculated to be greater than 2,300 suggesting turbulent flow. In the $k-\omega$ model, the turbulent kinetic energy $k$ and specific turbulent dissipation rate $\omega$ describe the turbulence of gas flow. The governing equations of the $k-\omega$ turbulence model are described in the SI. A representative CFD simulation of the gas flow distributions across the concrete block's surfaces within the carbonation reactor for the top flow direction is shown in Figure 2(a). The boundary conditions used in the simulations included the gas inlet velocity ($V_{inlet} = Q_{inlet}/A_{inlet}$) and outlet gas pressure ($P_{outlet} = 0$). The model's mesh consisted of 25,000 tetrahedral elements for the concrete blocks and 10,000 triangular elements for the reactor walls. The size of elements ranged from 0.005 m to 0.01 m for concrete block and reactor domains, respectively. To quantify the average contacting gas velocity and velocity non-uniformity, the gas flow field for every surface of the concrete block (see Figure 2b) was discretized into cells and their corresponding velocity magnitudes were extracted. The average contacting gas velocity across the i$^{th}$ surface of the concrete block $V_{ave,i}$ was then quantified as:

$$V_{ave,i} = \frac{\sum_{x=1}^{n} V_x}{n} \qquad \textbf{[Eq. 3]}$$

where $n$ is the number of cells (5 mm × 5 mm) on the block surface and $V_x$ corresponds to the velocity magnitude in each cell. To rationalize the data, in all cases, the average contacting gas velocity $V_{ave,i}$ was normalized by the gas inlet velocity $V_{inlet}$. The degree of non-uniformity (i.e., variation) of the contacting gas velocity across the block surfaces was then quantified as:

$$\text{Velocity Non-uniformity Index } = \frac{\sqrt{\frac{1}{n}\sum_{x=1}^{n}(V_x - V_{ave,i})^2}}{V_{ave,i}} \qquad \textbf{[Eq. 4]}$$

Thereafter, FEM analysis of the linear elastic behavior of the concrete block was carried out using COMSOL Multiphysics[33] to assess the effect of stiffness variations resulting from $CO_2$ uptake across the different block's sections on the overall mechanical response of the concrete block. The measured strength data of the block's sections was used to estimate material stiffness as an input in the FEM analysis as follows[47,48]:

$$E_{c,i} = k\sigma_{c,i} \quad \textbf{[Eq. 5]}$$

where $E_{c,i}$ (MPa) and $\sigma_{c,i}$ (MPa) are Young's modulus and compressive strength, respectively, of the i[th] section of the concrete block and $k$ is the coefficient relating elastic modulus to the compressive strength that was taken as 900 herein.[34] For dry-cast composites such as concrete blocks on account of their high aggregate contents, the elastic modulus is dictated by the stiffness of aggregate inclusions and degree of compaction.[36] As such, no distinction in elastic modulus is expected between traditional cement-based and carbonated concrete blocks. The estimated Young's moduli of the sections were input in the FEM analysis to simulate the concrete block (see Figure 2c). The governing equations of FEM analysis are detailed in the SI. To mimic compressive loading and minimize local stress concentrations, the steel bearing plates were modeled as well. As the boundary conditions, the displacements of the bottom plate were taken as zero in all directions (x, y, and z) and compressive stress was applied to the top surface by systematically increasing the applied stress from 0 to 15 MPa in 1.5 MPa increments. Perfect contact between the bearing steel plates and the surfaces of the concrete block was prescribed.

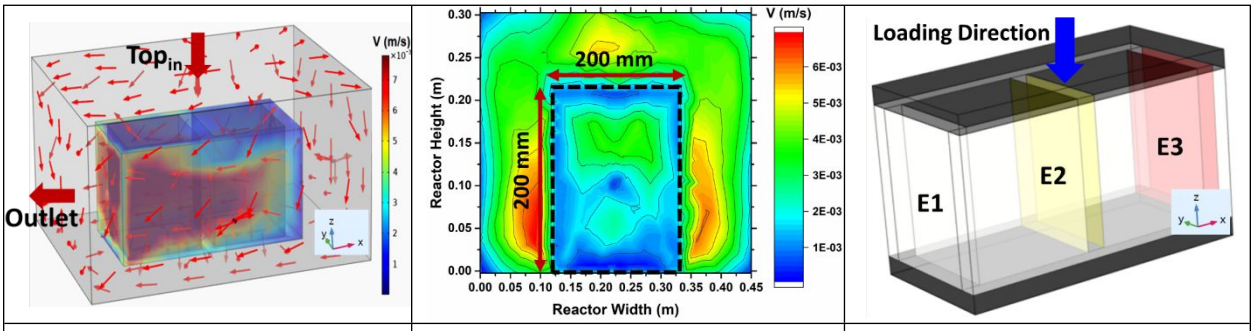


(a) (b) (c)

**Figure 2: (a)** CFD simulations of gas flow distributions across the concrete block's surfaces within the carbonation reactor for the top flow configuration. The velocity vectors within the reactor are shown as red arrows and the large arrows depict the gas inlet and outlet directions. **(b)** A contour plot of the gas velocity field across the surfaces of the concrete block (shown as dashed lines; outlet facing view). **(c)** FEM simulation of uniaxial compression of the carbonated block showing sections (i.e., sides, faces, and web) with different Young's moduli. The variations in Young's moduli of each section $E_{c,i}$ are shown in different colors.

## RESULTS AND DISCUSSION

**Effects of gas flow distribution on carbonation reaction:** The time-dependent $CO_2$ uptakes of different sections of the concrete blocks for different gas flow configurations were evaluated (see Figure 3). The $CO_2$ uptake was noted to vary significantly based on the gas flow configuration. Although all inlet faces featured nearly similar $CO_2$ uptake-time profiles (Figure 3a), the $CO_2$ uptake profiles of the outlet faces were expectedly impacted by the gas flow configuration (see Figure 3b). Unlike significant $CO_2$ uptake variations between different block's sections for both longitudinal and transverse flow configurations, the top flow featured the most uniform $CO_2$ uptake and the highest $CO_2$ uptake (see SI: Figure S3a). The overall 24-h $CO_2$ uptake was 0.089 $g_{CO2}/g_{reactants}$, 0.121 $g_{CO2}/g_{reactants}$, and 0.150 $g_{CO2}/g_{reactants}$ for the longitudinal, transverse, and top flow configurations, respectively. To quantify the effect of the flow

configuration on carbonation kinetics, the time-$CO_2$ uptake profiles were fitted to an equation of the form $C(t) = C(t_u)(1 - \exp[(-k_{carb}t)/C(t_u)])$ **[Eq. 6]**, where $k_{carb}$ is the apparent carbonation rate constant and $C(t_u)$ is the ultimate $CO_2$ uptake that was taken as the 24-h $CO_2$ uptake. Similar to $CO_2$ uptake, the carbonation rate constant for the different sections indicated a strong dependency on gas flow configuration. For instance, $k_{carb}$ for block's section facing the gas outlet was 4x lower than that of the inlet for the longitudinal direction, while near equivalent carbonation kinetics for both sections were observed for the top flow configuration.

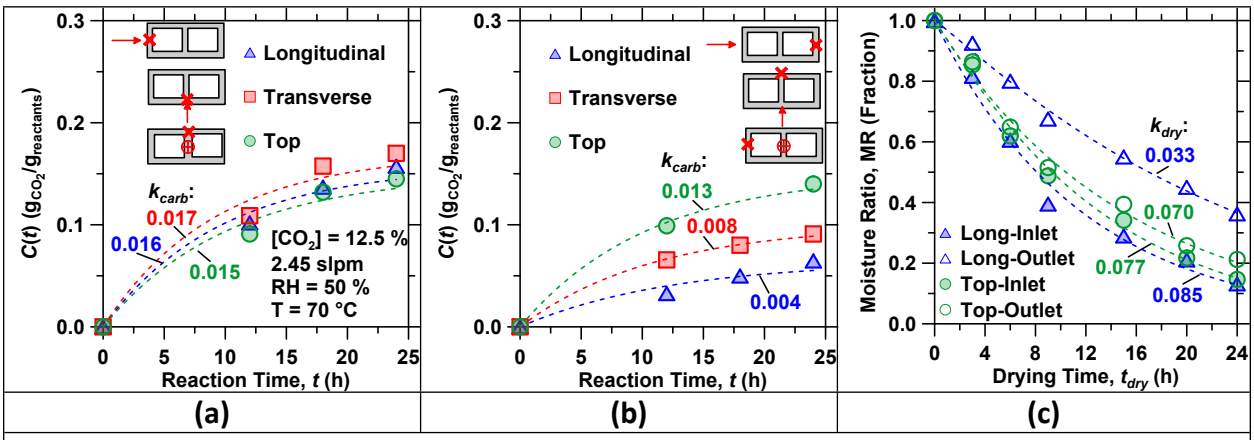


**Figure 3:** The time-dependent traces of the $CO_2$ uptake of the concrete block sections for different gas flow configurations for: **(a)** inlet and **(b)** outlet positions. The data was fitted to an equation of the form $C(t) = C(t_u)(1 - \exp[(-k_{carb}t)/C(t_u)])$. The insets depict the flow direction and sampling location (denoted by a cross) of the concrete block. In all cases, the gas stream featured [$CO_2$] = 12.5 %, *T* = 70 °C, *RH* = 50 %, and 2.45 slpm flow rate. **(c)** The evolution of the moisture ratio for different sections of the concrete block for varying gas flow configurations. The drying rate constant $k_{dry}$ was estimated by fitting the drying data to an equation of the form: $MR(t) = \exp[-k_{dry}t^n]$. During drying, the air stream featured [$CO_2$] = 0.04 %, *T* = 70 °C, *RH* = 50 %, and a flow rate of 2.45 slpm.

The suppression of carbonation kinetics across some of the block's sections is on account of higher water content in the block's pores (i.e., higher $S_w$) that was imposed by insufficient drying within sections whose surfaces are starved of gas flow. Our previous work has shown that the presence of water within the pores of microstructure inhibits carbonation by imparting $CO_2$ mass transfer resistance.[3] To assess the drying kinetics as a function of different gas flow configurations, the moisture ratio (MR) evolution was evaluated. To exclude the competing effects of carbonation and moisture transport, the concrete block was exposed to flowing air that was conditioned similarly (*T*, *RH*, and *Q*) to the carbonation experiments. The drying rate constant $k_{dry}$ was estimated as $MR(t) = \exp[-k_{dry}t^n]$ **[Eq. 7]**,[37] where $n$ is the fitting exponent and $MR(t)$ is the dimensionless moisture ratio at time $t$, which is given as $MR(t) = (\omega_t - \omega_e)/(\omega_0 - \omega_e)$ **[Eq. 8]**,[38,39] where $\omega_t$, $\omega_e$, and $\omega_0$ are moisture content at time $t$, the equilibrium moisture content, and initial moisture content, respectively. Generally, the drying rate $dMR(t)/dt$ decreases with time due to the transition from connected-liquid bridge drying to vapor diffusion as the drying front progressively penetrates deeper into the body.[40,41] In

agreement with the results of carbonation kinetics, the top flow configuration resulted in more uniform drying kinetics between inlet and outlet sections than that of the longitudinal flow (see Figure 3c). The similarity between carbonation and drying behavior of the concrete block's sections shows that the carbonation rate constant $k_{carb}$ is strongly correlated with and controlled by the drying rate constant $k_{dry}$ (see SI: Figure S3b), since enhanced drying facilitates $CO_2$ diffusion and thereby promotes the carbonation kinetics. This suggests that the variation of $CO_2$ uptake is induced on account of the different distributions of water content and drying front penetration across block's sections which affect gas diffusion (i.e., since gas diffusion in water ≈$10^4$ times slower than in air[29]).

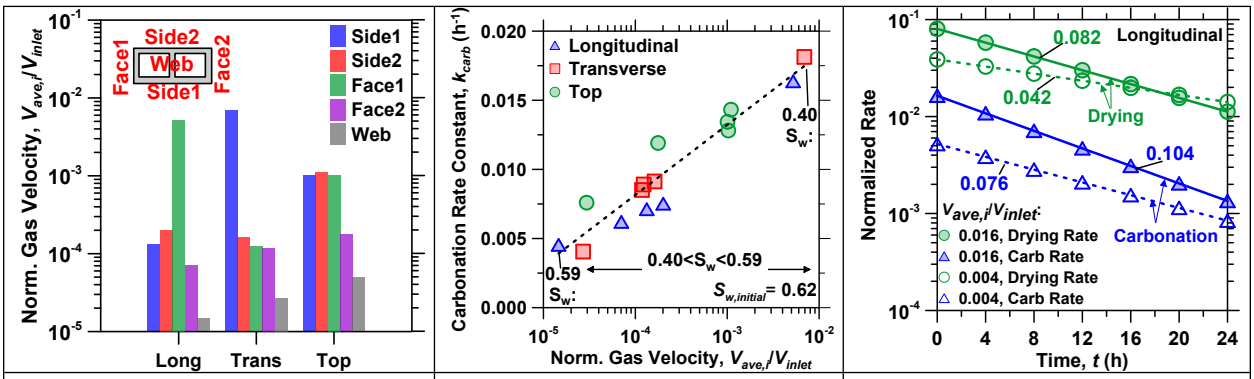


(a) (b) (c)

**Figure 4: (a)** CFD analysis of contacting gas velocity across different block's surfaces for varying gas flow configurations. **(b)** The evolution of the apparent carbonation rate constant $k_{carb}$ as a function of contacting gas velocity. Here, $k_{carb}$ was estimated using Eq. (6). The variation in pore saturation level $S_w$ with contacting gas velocity for different block's sections is also shown in **(b)**. The concrete block featured $S_{w,initial} = 0.62$ prior to the carbonation process. In all cases, the gas stream featured [$CO_2$] = 12.5 %, $T$ = 70 °C, $RH$ = 50 %, and 2.45 slpm flow rate. **(c)** Representative drying rate $dMR(t)/dt$ and carbonation rates $dC(t)/dt$ traces at different contacting gas velocities.

The variations in drying kinetics across the different sections of the block are attributed to the spatial variations of the contacting gas velocity. Indeed, our CFD analysis revealed that the top flow configuration resulted in the most-spatially uniform and the highest average velocity across block's surfaces (see Figure 4a). This explains the more uniform and higher $CO_2$ uptake for the top flow configuration. The evolution of carbonation rate constant $k_{carb}$ showed a logarithmic scaling as a function of contacting gas velocity (Figure 4b). This suggests that the overall carbonation reaction rate is controlled by the overall drying rate, since a higher drying rate enhances the penetration of the drying front*, as evidenced by the reduced $S_w$ from 0.62 to 0.40. In turn, increasing the contacting gas velocity by 3 orders of magnitude resulted in a proportionate 3.5x enhancement of carbonation rate (Figure 4b). Independent of the gas flow

* The term "drying front" is generically defined as the interface between fully saturated and partially saturated regions.[40–42] We use this term here to indicate the transition zone between regions that have a reduced pore saturation as compared to the initial pore saturation level of a concrete block ($S_{w,initial} = 0.62$).

configuration, the contacting gas velocity diminished significantly within the web section. This resulted in the lowest carbonation level among all sections of the concrete block (see Figure 4a) in the occluded web. This is on account of the low length-to-depth ratio ($L/D = 1$) of the concrete block's hollows, as a result of which marginal flow occurs within the core-sections suggesting the formation of dead regions ($V \approx 0$).[43]

A greater initial drying rate and faster drying resulted in a greater carbonation rate at early ages followed by a faster decrease in the carbonation rate as evidenced by the profiles in Figure 4(c). Although the rate of penetration of the drying front increases with gas velocity, the enhanced formation of carbonate minerals ($CaCO_3$) in the direction of the drying front can produce blockages in the microstructure. This can impose an additional transport limitation that can suppress the carbonation rate at later reaction times. It is important to note that the effect of the contacting gas velocity on moisture transfer within the pore spaces is also affected by the gas processing conditions (*T* and *RH*). For instance, for a given contacting gas velocity, increasing the *RH* of the gas stream slows moisture transport and penetration of drying front due to the competition between inward and outward transport of (condensed) moisture within the pores, as discussed in the next section.

**Effects of interactions between gas processing conditions on carbonation reaction:** For a given gas flow configuration, the carbonation of concrete components is strongly influenced by the gas processing parameters (*T*, *RH*, and *Q*). To systematically assess such effects and their interactions, a factorial Design-of-Experiments (DoE) approach was used to generate response surfaces and derive statistical prediction models. To vary the initial pore saturation level $S_{w,initial}$, the blocks were initially dried by exposure to flowing air prior to the carbonation process. The ANOVA results are presented in Table S3 in SI, which indicates the significant parameters and interactions. As an example, the response surface of $CO_2$ uptake visualizes the combined effect of *RH* and *Q* of gas (see Figure 5a). The statistical models for $S_w$ after drying and 24-h $CO_2$ uptake of concrete blocks were derived as:

$$S_{w,idrying} = 0.62890 - 0.00397 \times T + 0.00198 \times RH - 0.07348 \times Q_i + 0.00111(RH \times Q_i) \quad \textbf{[Eq. 9]}$$

$$C(24h)_i = -0.00592 + 0.00127 \times T - 0.00022 \times RH + 0.04373 \times Q_i - 0.00064(RH \times Q_i) \quad \textbf{[Eq. 10]}$$

The significant parameters and interactions were found to be identical between both responses, although having opposite signs, demonstrating the significance of $S_w$ as a dominant variable that affects the carbonation of concrete components. Hereafter, to predict the $CO_2$ uptake of the different block's sections, the variations in the contacting gas velocity as a function of gas inlet flow rate were determined using CFD analysis. Increasing the flow rate at the gas inlet enhanced the contacting gas velocity and improved the velocity uniformity across different block's surfaces (see Figure 5b). For a given block surface, the correlation between normalized contacting velocity and gas flow rate can be described by the power function of the form $V_{ave,i}/V_{inlet} = aQ_i^b$ **[Eq. 11]**, where $a$ and $b$ are fitting parameters that depend on the concrete block section (see Figure 5b). Knowledge of the normalized contacting gas velocity and

the corresponding gas flow rate $Q_i$ (using Eq. 11), allows prediction of the average $CO_2$ uptake for a given concrete block's section using Eq. 10; for this specific reactor configuration.

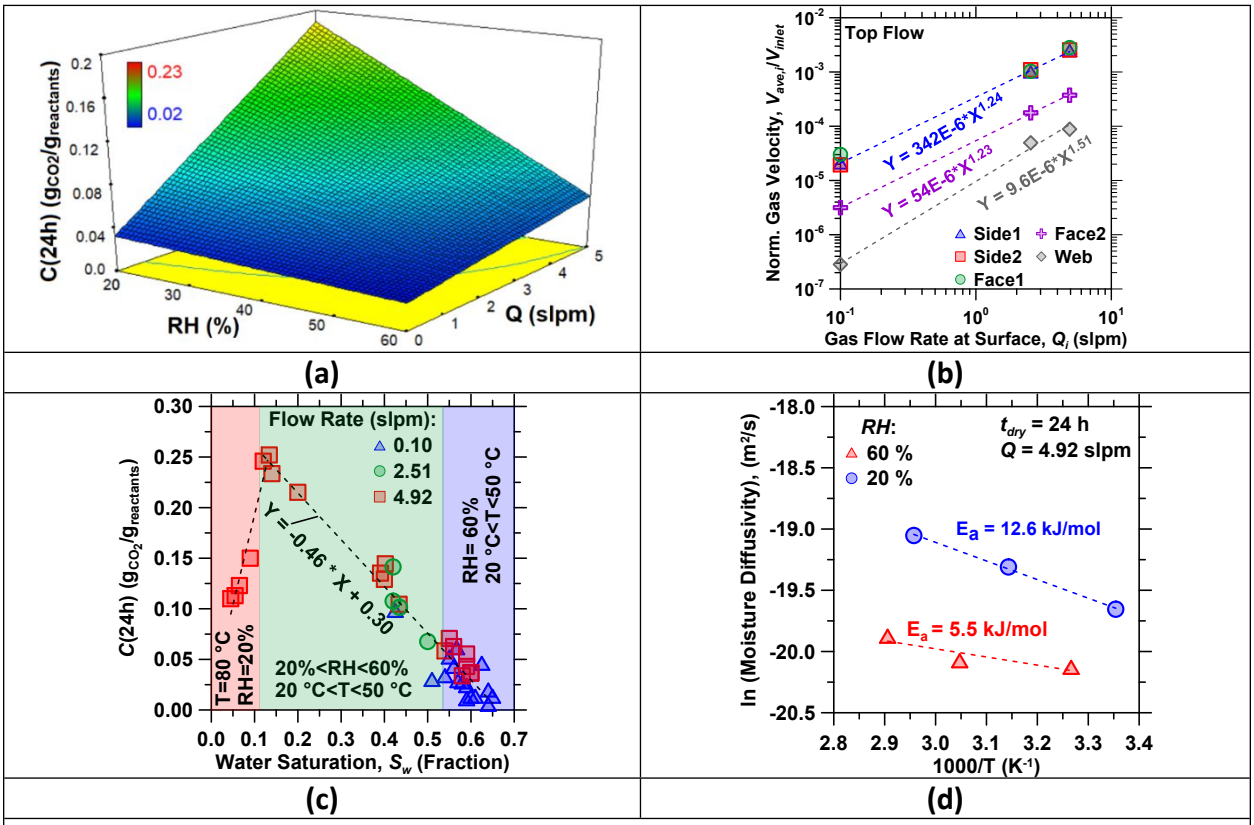


**Figure 5: (a)** Response surface of the 24-h $CO_2$ uptake of the concrete block under different *RH* and *Q* of gas at *T* = 35 °C. **(b)** The variations of contacting gas velocity (determined by CFD analysis) as a function of *Q* for different block's surfaces. **(c)** The variations in 24-h $CO_2$ uptake as a function of initial pore water saturation $S_w$ after the drying step. The shaded regions in **(c)** represent different processing conditions. In all cases, the concrete blocks were initially dried by exposure to flowing air prior to the carbonation process. **(d)** Arrhenius plots of the activation energy of moisture diffusion ($E_a$) at different gas *RH* during drying. Herein, all the data corresponds to the "top flow" configuration.

Coming back to pore water saturation, the 24-h $CO_2$ uptake of the block sections was noted to scale with $S_{w,drying}$ (see Figure 5c), as estimated by a linear function of the form $C(24h)_i = -0.46 \times S_{w,i} + 0.30$ for $S_w > 0.11$ **[Eq. 12]**. It should be noted that this equation is valid only for the design space considered herein. For instance, it has been previously noted that critical $S_{w,c} \approx 0.10$ is required to sustain the dissolution-carbonation reaction of portlandite.[3,9] To capture this breakpoint, a separate dataset (outside the design space) was collected under aggressive drying at *T* = 80 °C and *RH* = 20 % that revealed that $CO_2$ uptake was substantially suppressed when $S_w$ dropped below 0.11. This is significant since it indicates that (Eqs. 9, 10, and 12) are valid for $S_w > S_{w,c} \approx 0.10$. The $CO_2$ mineralization mechanism via portlandite carbonation within concrete monoliths proceeds via a dissolution-precipitation pathways including[4]: (i)

release of $Ca^{2+}$ species into the pore liquid due to dissolution of alkaline reactants, (ii) transport and dissolution of $CO_2$ though and within the monolith's pore network, and (iii) precipitation of carbonate minerals via combination of dissolved species ($Ca^{2+}$, $CO_3^{2-}$, and $HCO_3^-$). It should be noted, however, that a critical moisture saturation level ($S_{w,c} \approx 0.10$) is required to sustain the carbonation reaction.[3,9] So long as $S_{w,c}$ is exceeded, $Ca^{2+}$ species liberated following the dissolution of portlandite react with dissolved $CO_2$ species (i.e., $CO_3^{2-}$ and $HCO_3^-$) to precipitate calcium carbonate.[44,45]

Further, limited $CO_2$ uptake was noted when gas *RH* was similar to the initial $S_w = 0.62$ of the concrete block (see the shaded blue region in Figure 5c). This is attributed to a small driving force for evaporation, and a balance between moisture transport into and out of the pore structure, such that drying is hindered. This was evidenced by quantifying the apparent activation energy of moisture diffusion (see Figure 5d). Indeed, Arrhenius analysis of moisture diffusivity at *RH* = 60 % shows a small dependence on temperature as compared to moisture diffusion at *RH* = 20 %. In general, the small apparent activation energy (<20 kJ/mol) is reflective of limited temperature sensitivity for drying of the monoliths; and indicates a transport-controlled, i.e., rather than surface reaction-controlled process. Accordingly, at *RH* = 60 % ($E_a \approx$ 5.5 kJ/mol), wherein the contacting gas's relative humidity is similar to the pore water saturation of the concrete block ($S_w$ = 0.62), drying is hindered due to the similar rates of moisture transfer inward from the ambient environment and outward from pore network. As the RH of the contacting gas stream is reduced, moisture removal becomes somewhat more sensitive to temperature (e.g., a 3x reduction in the RH translates to only a doubling of the activation energy). Unsurprisingly, the activation energies of moisture diffusion noted herein are considerably lower than that reported for mature, hardened cement paste (e.g., ≈ 32-45 kJ/mol for water-to-cement ratio = 0.40-0.60[46,47]); under conditions where no air-flow occurred. The smaller temperature dependence ($E_a$) of moisture diffusivity in the presence of air flow is likely because air flow facilitates moisture transport due to a sharper, and sustained *RH* gradient between the ambient vapor and the monolith's surface from where evaporation occurs. These findings reinforce the premise that both optimal reactor (gas) flow distribution and gas processing conditions are critical to enhancing carbonation kinetics and carbonation uniformity within concrete components.

**Effects of gas flow distribution on carbonation strengthening:** The strengthening of concrete components during $CO_2$ exposure is affected by cement hydration, pozzolanic, and carbonation reactions.[3] As the extent of $CO_2$ uptake determines carbonate cementation,[1,3] variations in $CO_2$ uptake can induce non-uniformity in carbonation strengthening, which can impact the overall mechanical response of carbonate-cemented components. Herein, it was noted that the porosity of carbonated samples, that were extracted from different sections of the concrete block, demonstrated a sigmoidal/tri-linear refinement with $CO_2$ uptake (see Figure 6a). On account of more uniform $CO_2$ uptake, the top flow configuration resulted in a lower porosity and smaller variations in porosity across different block's sections as compared to the longitudinal and transverse flow directions. The tri-linear trend indicated a secondary slope $m_2 = 76.6$ (i.e., between 0.05 $g_{CO2}/g_{reactants}$ and 0.15 $g_{CO2}/g_{reactants}$) that was substantially steeper

than the first and third slopes ($m_1 = 6.7$ and $m_3 = 3.5$) on account of the enhanced formation of space-filling carbonate products. The smaller slope $m_1$ is attributed to the small extent of cement hydration ($w_n/m_{\mathrm{OPC}}$) and minimal carbonation. The smallest slope $m_3$ results from a near-complete conversion (i.e., carbonation) of portlandite (≈85 % based on TGA analysis) which is the primary reactant used for $CO_2$ mineralization in the concrete monolith. As a result, the contribution of carbonation to porosity refinement saturates as portlandite carbonation reaches the final conversion extent. To exclude the effect of cement hydration, the compressive strength results were normalized by $w_n/m_{\mathrm{OPC}}$ and plotted as a function of $CO_2$ uptake (see Figure 6b). Interestingly, $\sigma_c/(w_n/m_{\mathrm{OPC}})$ enhanced exponentially with an exponent of 8.72 per unit mass of $CO_2$ uptake, confirming that strengthening offered by carbonation is foundational in ensuring the strength gain of the structural component. Additionally, the extrapolation of the curve to determine the y-intercept (see solid line in Figure 6b) yielded nearly an equivalent value to that of uncarbonated concrete block suggesting that carbonation does not detrimentally affect the strength gain resulting from cement hydration.

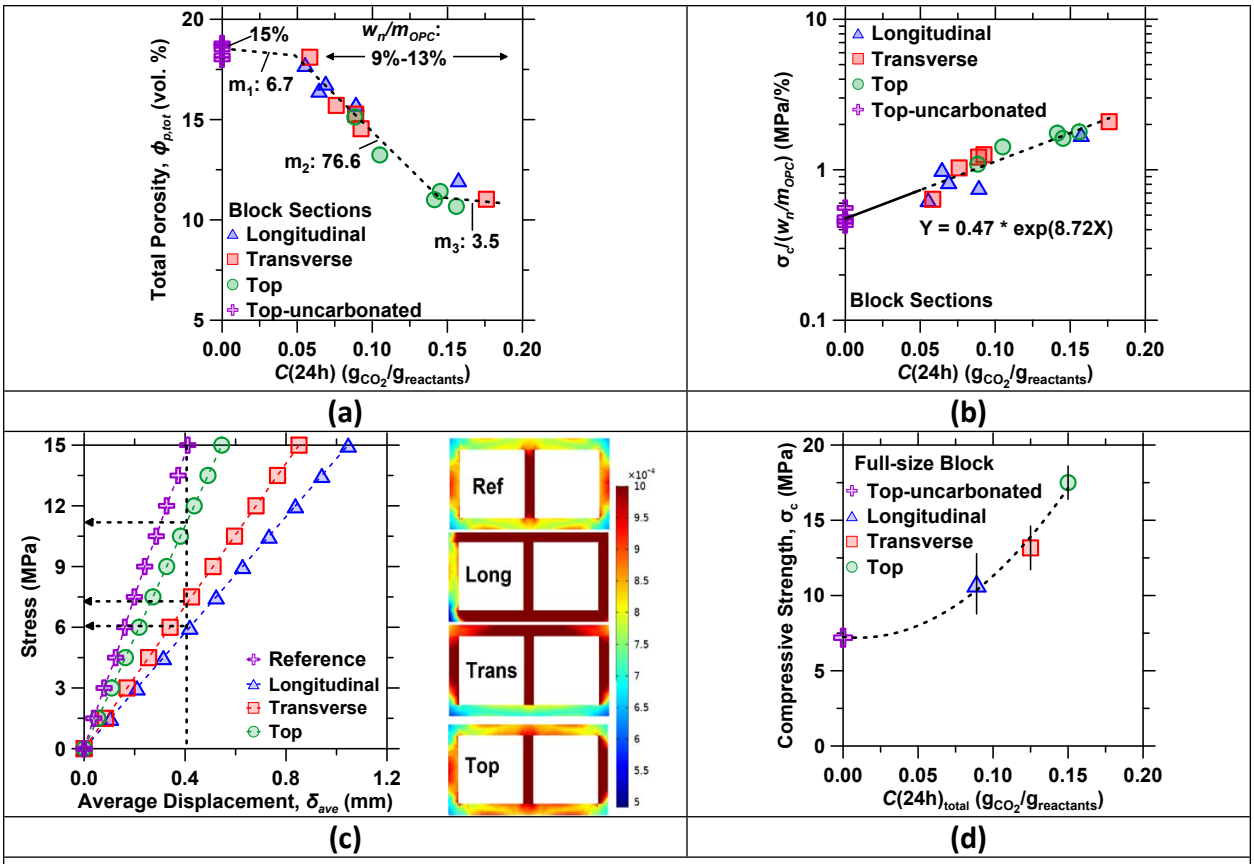


**Figure 6: (a)** The variations in porosity across different sections of carbonated blocks as a function of $CO_2$ uptake under different gas flow configurations. **(b)** The normalized strength evolution as a function of the $CO_2$ uptake for different sections of concrete blocks. **(c)** The FEM analysis of the uniaxial compressive stress-displacement response of carbonated concrete blocks. The Young's modulus of every section was estimated using [Eq. 5]. The reference concrete block was modeled using a homogenous Young's modulus of 14 GPa.[34]

Strain distributions across top surfaces of concrete blocks at $\sigma_c = 15$ MPa are shown. **(d)** The variations in the measured compressive strengths of concrete blocks as a function of overall $CO_2$ uptake for different gas flow configurations. During carbonation, the gas stream featured [$CO_2$] = 12.5 %, *T* = 70 °C, *RH* = 50 %, and 2.45 slpm flow rate.

On account of the lowest $CO_2$ uptake, the smallest compressive strength was noted for the web sections of carbonated concrete block. The variations in material strength and elastic properties across the concrete block's sections can result in non-uniform stress and displacement distributions under loading. This is confirmed by FEM simulations of the stress-displacement response of concrete blocks (see Figure 6c). In contrast to top flow, concrete blocks carbonated under the longitudinal and transverse flow directions featured far more non-uniform strain distributions, and as a result, the compressive strength reduced from 15 MPa to 6 MPa for a given displacement of 0.4 mm. Based on the displacement analysis for the reference concrete block with uniform Young's modulus, the web section experienced the largest deformation as compared to the other sections (see Figure 6c and Figure S7 in SI). This is in agreement with other studies wherein the failure of CMUs usually occurs when the web section cracks.[48,49] In analogous to traditional cement-based blocks, therefore, the web section which experiences the lowest $CO_2$ uptake dictates the overall mechanical response in carbonated concrete blocks. In agreement with the FEM simulations, the measured compressive strengths of the concrete blocks were noted to be affected by gas flow distribution and correlated with overall $CO_2$ uptake (see Figure 6d). Importantly, the failure mode of concrete blocks was noted to vary from "conical" failure for top flow to "conical/shear" failure for longitudinal and transverse flow configurations in accordance with failure modes described in ASTM C1314.[50] Expectedly, more cracking was observed in the less-carbonated sections (e.g., web) of the blocks. This is thought to result from variations in material strength/stiffness properties that strongly dictate the failure mode by inducing shear/tension cracks along with the weakest zones.[62,63]Therefore, the reduced compressive strength of less-carbonated blocks is linked to the combined effects of non-uniformity of material elastic properties and the reduced carbonation strengthening contribution.

## IMPLICATIONS FOR THE DESIGN OF $CO_2$ MINERALIZATION REACTORS AND PROCESSES

The CFD modeling carried out herein allows analysis of the spatial distribution and velocity of contacting gas to inform the optimal: (a) design of gas flow distribution systems and (b) geometrical arrangement of concrete components within a $CO_2$ mineralization reactor's volume so as to maximize and ensure the uniformity of $CO_2$ uptake of low-carbon concrete products. These aspects are particularly related to how variations in the contacting gas velocity affect drying, drying gradients, and consequently $CO_2$ uptake gradients within a monolith's volume. The outcomes of this work, importantly, offer a basis of extension to other component geometries, e.g., other than the concrete block, which feature varying thicknesses and surface-to-volume ratios, i.e., to expand the palette of products that can be produced via $CO_2$ mineralization processes. In addition, the CFD simulations carried out herein, form the basis for the development of a fully coupled heat-mass-chemical reaction-transport model that is required to comprehensively relate aspects of binder composition, gas processing conditions (e.g., *T*, *RH*, [$CO_2$], and *Q*), reactor geometry, component geometry, and $CO_2$ (mineralization)

uptake, to each other so as to maximize direct $CO_2$ utilization using industrial flue gas emission streams, in a time-, cost- and energy-efficient manner.

## SUMMARY AND CONCLUSIONS

This study has elaborated on how gas flow distributions within a plug-flow style reactor affect $CO_2$ uptake and the resulting carbonate cementation of monolithic concrete components (i.e., herein concrete masonry units: CMUs, also known as the concrete block). Special focus was paid to uncover how drying kinetics and liquid water distributions, resulting from varying gas flow distributions, impact the rate and extent of carbonation. The dependence of carbonation kinetics on the contacting gas velocity is attributed to the variation in drying kinetics and the penetration rate of drying front (i.e., $S_w$ gradients) which affect the microstructural resistance to gas diffusion. Such $S_w$ gradients result in non-uniform $CO_2$ uptake across the monolith's volume, which imposes gradients in material properties (e.g., porosity and stiffness), and thereby impacts the overall mechanical response of carbonate-cemented concrete components. Both CFD and FEM simulations were used to assess the effects of the spatial distribution of contacting gas velocity across a concrete block's surfaces on variations in $CO_2$ uptake within concrete block's sections and resultant material properties (stiffness and strength). Finally, for the optimal gas flow configuration, the effects of gas processing conditions (*RH*, *T*, and *Q*) on $CO_2$ mineralization reactions of the concrete block were highlighted. The understanding gained is critical to inform the optimal design of $CO_2$ mineralization systems and the selection of gas processing routes to enhance and to ensure uniformity of $CO_2$ uptake and material properties evolution within concrete components. The outcomes are of relevance to design optimal carbonation systems, and to manufacture low-$CO_2$ concrete components that utilize waste $CO_2$ borne in flue gas streams and fulfill relevant construction standards, without a need for a carbon capture step, and at ambient pressure.

## ACKNOWLEDGEMENTS

The authors acknowledge financial support for this research from the Department of Energy: Office of Fossil Energy via the National Energy Technology Laboratory (NETL; DE-FE0029825 and DE-FE0031718), The Anthony and Jeanne Pritzker Family Foundation, and the National Science Foundation (DMREF: 1922167). This research was conducted in the Laboratory for the Chemistry of Construction Materials ($LC^2$) at UCLA. The authors gratefully acknowledge the support provided by these laboratories. The contents of this paper reflect the views and opinions of the authors, who are responsible for the accuracy of the datasets presented herein, and do not reflect the views and/or policies of the funding agencies, nor do the contents constitute a specification, standard or regulation.

## SUPPORTING INFORMATION

Oxide composition of binders, concrete block forming process, factorial Design-of-Experiment, sampling procedure for $CO_2$ uptake characterization, CFD and FEM governing equations, $CO_2$ uptake variations, CFD simulations of contacting gas velocity, derivation of statistical prediction models, desirability response for multivariable optimization, and FEM analysis of the uniaxial compressive response of concrete block.

## REFERENCES

1 Z. Wei, B. Wang, G. Falzone, E. C. La Plante, M. U. Okoronkwo, Z. She, T. Oey, M. Balonis, N. Neithalath and L. Pilon, *Journal of CO2 Utilization*, 2018, **23**, 117–127.

2 National Academies of Sciences, Engineering, and Medicine, *Gaseous Carbon Waste Streams Utilization: Status and Research Needs*, The National Academies Press. https://doi.org/10.17226/25232, Washington, DC, 2018.

3 I. Mehdipour, G. Falzone, E. C. La Plante, D. Simonetti, N. Neithalath and G. Sant, *ACS Sustainable Chemistry & Engineering*, 2019, **7**, 13053–13061.

4 K. Vance, G. Falzone, I. Pignatelli, M. Bauchy, M. Balonis and G. Sant, *Industrial & Engineering Chemistry Research*, 2015, **54**, 8908–8918.

5 S.-Y. Pan, B. Lai and Y. Ren, *RSC Advances*, 2019, **9**, 31052–31061.

6 S.-Y. Pan, Y.-H. Chen, L.-S. Fan, H. Kim, X. Gao, T.-C. Ling, P.-C. Chiang, S.-L. Pei and G. Gu, *Nature Sustainability*, 2020, **3**, 399–405.

7 G. Habert, S. A. Miller, V. M. John, J. L. Provis, A. Favier, A. Horvath and K. L. Scrivener, *Nature Reviews Earth & Environment*, 2020, **1**, 559–573.

8 E. Gartner and T. Sui, *cement and concrete research*, 2018, **114**, 27–39.

9 S.-M. Shih, C.-S. Ho, Y.-S. Song and J.-P. Lin, *Industrial & engineering chemistry research*, 1999, **38**, 1316–1322.

10 D. T. Beruto and R. Botter, *Journal of the European Ceramic Society*, 2000, **20**, 497–503.

11 V. Baroghel-Bouny, *Cement and Concrete Research*, 2007, **37**, 414–437.

12 X.-Y. Gao, G.-W. Chu, Y. Ouyang, H.-K. Zou, Y. Luo, Y. Xiang and J.-F. Chen, *Industrial & Engineering Chemistry Research*, 2017, **56**, 14350–14361.

13 X. Shi, Y. Xiang, L.-X. Wen and J.-F. Chen, *Industrial & engineering chemistry research*, 2012, **51**, 13944–13952.

14 R. G. Szafran and A. Kmiec, *Industrial & engineering chemistry research*, 2004, **43**, 1113–1124.

15 M. Kim, J. Na, S. Park, J.-H. Park and C. Han, *Chemical Engineering Science*, 2018, **177**, 301–312.

16 A. G. Dixon and M. Nijemeisland, *Industrial & Engineering Chemistry Research*, 2001, **40**, 5246–5254.

17 *ASTM C150/C150M − 18: Standard Specification for Portland Cement*, ASTM International, West Conshohocken, PA, 2018.

18 *ASTM C618 − 15: Standard Specification for Coal Fly Ash and Raw or Calcined Natural Pozzolan for Use in Concrete*, ASTM International, West Conshohocken, PA, 2015.

19 *ASTM C90 - 16a: Standard Specification for Loadbearing Concrete Masonry Units*, ASTM International, West Conshohocken, PA, 2016.

20 *ASTM C140/C140M − 18a: Standard Test Methods for Sampling and Testing Concrete Masonry Units and Related Units*, ASTM International, West Conshohocken, PA, 2018.

21 G. T. Rochelle, *Science*, 2009, **325**, 1652–1654.

22 D. C. Montgomery, *Design and analysis of experiments*, John wiley & sons, 2017.

23 G. Derringer and R. Suich, *Journal of quality technology*, 1980, **12**, 214–219.

24 *ASTM C1872 − 18: Standard Test Method for Thermogravimetric Analysis of Hydraulic Cement*, ASTM International, West Conshohocken, PA, 2018.

25 I. Pane and W. Hansen, *Cement and concrete research*, 2005, **35**, 1155–1164.

26 A. Arora, G. Sant and N. Neithalath, *Construction and Building Materials*, 2016, **102**, 113–124.

27 F. Montes, S. Valavala and L. M. Haselbach, *Journal of ASTM International*, 2005, **2**, 1–13.

28 *ASTM C39/C39M − 18: Standard Test Method for Compressive Strength of Cylindrical Concrete Specimens*, ASTM International, West Conshohocken, PA, 2018.

29 J. Crank, *The mathematics of diffusion*, Oxford university press, 1979.

30 C. Comsol, *4.3 CFD Module User's guide*, DOI, 2012.

31 D. C. Wilcox, *Turbulence modeling for CFD*, DCW industries La Canada, CA, 1998, vol. 2.

32 C. Multiphysics and C. Module, *Version: COMSOL Multiphysics*.
33 A. B. Comsol, *Structural mechanics module user's guide*, Comsol AB, Stockholm, 2012.
34 M. S. J. Committee, *The Masonry Society, Boulder, CO*.
35 G. Mohamad, P. B. Lourenço and H. R. Roman, *Cement and Concrete Composites*, 2007, **29**, 181–192.
36 D. W. Hobbs, *Matériaux et construction*, 1971, **4**, 107–114.
37 G. E. Page, .
38 K. Sacilik, *Journal of food engineering*, 2007, **79**, 23–30.
39 A. Midilli, *International Journal of Energy Research*, 2001, **25**, 715–725.
40 G. W. Scherer, *Journal of the American Ceramic Society*, 1990, **73**, 3–14.
41 J. Van Brakel, *Powder technology*, 1975, **11**, 205–236.
42 P. Lehmann, S. Assouline and D. Or, *Physical Review E*, 2008, **77**, 056309.
43 B. John, X.-J. Gu and D. R. Emerson, *Computers & fluids*, 2011, **45**, 197–201.
44 S.-M. Shih, C.-S. Ho, Y.-S. Song and J.-P. Lin, *Industrial & engineering chemistry research*, 1999, **38**, 1316–1322.
45 D. T. Beruto and R. Botter, *Journal of the European Ceramic Society*, 2000, **20**, 497–503.
46 C. Page, N. R. Short and A. El Tarras, *Cement and concrete research*, 1981, **11**, 395–406.
47 H. Takiya, N. Watanabe, T. Kozaki and S. Sato, *Journal of nuclear science and technology*, 2015, **52**, 728–738.
48 M. S. Jaafar, A. H. Alwathaf, W. A. Thanoon, J. Noorzaei and M. R. Abdulkadir, *Proceedings of the Institution of Civil Engineers-Construction Materials*, 2006, **159**, 111–117.
49 G. G. C. Ngapeya, D. Waldmann and F. Scholzen, *Construction and Building Materials*, 2018, **165**, 898–913.
50 *ASTM C1314 − 18: Test Method for Compressive Strength of Masonry Prisms*, ASTM International, West Conshohocken, PA, 2018.
51 A. W. Hendry, *Structural masonry*, Macmillan International Higher Education, 1998.
52 L. Berto, A. Saetta, R. Scotta and R. Vitaliani, *Materials and structures*, 2005, **38**, 249–256.